ACS APPLIED MATERIALS & INTERFACES

www.acsami.org Research Article

Enhancing the Properties of Yttria-Stabilized Zirconia Composites with Zeolitic Imidazolate Framework-Derived Nanocarbons

Niyaz Cakan,[▽] Abduselam Abubeker Issa,[▽] Hamza Alsalman,[▽] Emin Aliyev,[▽] Enes Ibrahim Duden, Kubra Gurcan Bayrak, Mujdat Caglar, Servet Turan, Mustafa Erkartal,* and Unal Sen*

Cite This: *ACS Appl. Mater. Interfaces* 2023, 15, 58931−58939 Read Online

ACCESS | Metrics & More | Article Recommendations | Supporting Information

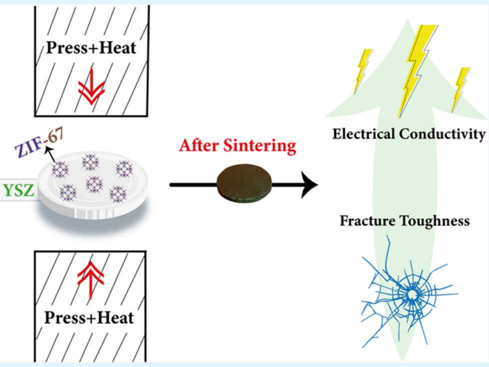

ABSTRACT: Ceramic matrix composites (CMCs) reinforced with nanocarbon have attracted significant interest due to their potential to enhance mechanical, thermal, and electrical properties. Although the investigation of carbon-based materials such as graphene and carbon nanotubes as additives for advanced ceramics has been widespread, the utilization of metal−organic framework (MOF)-derived nanocarbons in CMCs remains largely unexplored. We extended our previous proof-of-concept investigations by demonstrating the effectiveness of a different type of MOF-derived carbon as a reinforcing phase in an alternative ceramic matrix. We employed spark plasma sintering (SPS) to consolidate yttria-stabilized zirconia (YSZ) and zeolitic imidazolate framework (ZIF-67) powder blends at 1300 °C and a uniaxial pressure of 50 MPa. YSZ serves as the ceramic matrix, whereas ZIF-67 serves as the nanocarbon source. The composite exhibits a highly significant improvement in fracture toughness with an increase of up to 13% compared to that of the YSZ monolith. The formation of ZIF-derived nanocarbon interlayers is responsible for the observed enhancement in ductility, which can be attributed to their ability to facilitate energy dissipation during crack propagation and inhibit grain growth. Furthermore, the room-temperature electrical conductivity of the sintered samples demonstrates a substantial improvement, primarily due to the in situ formation of nanocarbon-based fillers, reaching an impressive 27 S/m with 10 wt % ZIF-67 content. Based on the results, it can be inferred that the incorporation of in situ MOF-derived nanocarbons into CMCs leads to a substantial improvement in both the mechanical and electrical properties.

KEYWORDS: *ceramic matrix composites, metal−organic framework-derived nanocarbons, zeolitic imidazolate framework, yttria-stabilized zirconia, spark plasma sintering*

1. INTRODUCTION

Ceramics are very important engineering materials due to their exceptional properties, including high-temperature stability, mechanical strength, and resistance to harsh environmental conditions.[1] However, to meet the ever-evolving demands of modern technology and industry, there is a compelling need for the further development of ceramic-based materials. In this field, nanocarbon-reinforced ceramic matrix composites (CMCs) have emerged as the focus of research and innovation, promising a paradigm shift in the field of advanced materials.[2,3] These composites combine the intrinsic strengths of ceramics, such as high-temperature stability and corrosion resistance, with the remarkable properties of nanocarbon materials, such as outstanding electrical conductivity, mechanical strengthening, and multifunctionality.[4,5] Therefore, due to their superior properties, nanocarbon-reinforced CMCs have gained widespread acceptance due to their potential to revolutionize numerous applications ranging from aerospace and automotive industries to electronics and energy conversion systems.[5]

The incorporation of nanocarbon materials, including graphene,[6−8] carbon nanotubes (CNTs),[9,10] and carbon nanofibers (CNFs),[11,12] into ceramic matrices has displayed immense potential, and overcoming persistent challenges related to nanocarbon agglomeration, interfacial incompatibility, and various issues associated with ceramic fabrication methods remains a significant obstacle. High surface area and energy, as well as van der Waals forces from intermolecular electrical dipoles, lead to agglomeration of nanocarbons, which in turn limits the dispersion of nanocarbons in a ceramic matrix and diminishes the mechanical properties.[13] In addition, owing to the vastly different densities and surface tensions of nanocarbons and ceramics, interfacial incompatibility further limits the properties of carbon-enhanced ceramics.[14] Another

Received: October 13, 2023
Revised: November 29, 2023
Accepted: November 29, 2023
Published: December 9, 2023

https://doi.org/10.1021/acsami.3c15359
ACS Appl. Mater. Interfaces 2023, 15, 58931−58939

common challenge is fabrication difficulties, such as controlling the temperature during the sintering process, which can weaken the interfacial bond of the composite.[15] These difficulties can be overcome by uniformly blending the carbon source with the ceramic in the solid phase and subsequently subjecting it to carbonization during sintering.

Metal−organic frameworks (MOFs) are crystalline/amorphous porous frameworks that consist of metal ions or clusters that bond with organic linkers that typically bear chelating functionalities that favor the formation of polynuclear secondary building units (SBUs).[16−18] Owing to their tunable nature, which can be manipulated to achieve high surface areas, MOFs have solidified their application potential for gas storage,[19,20] separation,[21,22] catalysis,[23−26] and electrochemical applications.[27,28] In addition to MOFs being promising materials for many applications in their crystalline state, researchers have shown the potential of MOFs for designing metal-based and carbon-based nanocomposites by pyrolysis and controlling the morphology and structure of the derived carbon by manipulating the pyrolysis conditions and components of the MOF.[29,30]

Previously, our research successfully showcased the value of MOF as a source of nanocarbon reinforcement in CMCs through the use of spark plasma sintering (SPS), a highly effective powder consolidation method.[31] Our findings indicated that when zeolitic imidazolate framework (ZIF-8) nanopowder was uniformly dispersed within an Al_2O_3 matrix in solid form, it underwent an in situ transformation into graphitic carbon during the sintering process. The resulting composites exhibited notably enhanced fracture toughness and electrical conductivity relative to pure sintered Al_2O_3.[31] Building upon this innovative concept, this study extends its application to other ceramic matrices and MOFs. In this context, we used YSZ as the matrix material for the CMCs investigated in this study. Zirconia (ZrO_2) is an attractive ceramic material for biomedical, structural, and high-temperature applications, owing to its exceptional chemical stability.[32] While pure zirconia has drawbacks such as poor crack growth resistance and low fracture toughness, the addition of just 3 mol % yttria (Y_2O_3) eliminates these weaknesses as a result of the phase transformation toughening phenomenon.[33] Nevertheless, multiple phase transformations might lead to excessive volume expansion and consequently lead to the failure of YSZ.[34] To overcome this, researchers have used reinforcement materials with different morphologies, and it has been reported that the homogeneous distribution of the reinforcing phase in the ceramic matrix reduces the local stress fields and suppresses crack growth and propagation, which in turn subdues the aforementioned stress-induced phase transformation.[35] ZIF-67, which is composed of cobalt ions (Co^{2+}) and 2-methylimidazolate linkers, was used as the nanocarbon source for the reinforcement phase. It possesses a substantial surface area exceeding 1700 $m^2\ g^{-1}$, which imparts ZIF-67 with an abundance of active sites. Furthermore, derivatives such as metal oxides and metal/carbon composites obtained by pyrolysis of ZIF-67 have the potential to introduce new properties not present in the pristine ZIF-67 structure and have therefore been utilized in CO_2 capture and electrochemical applications.[36]

2. MATERIALS AND METHODS

2.1. Preparation of YSZ and ZIF-67 Hybrid Powders. Commercial chemicals were used without additional purification unless otherwise specified. High-purity YSZ powder YSZ (ZrO_2−3 mol % Y_2O_3) with a purity of 99.8% was purchased from Tosoh Co., Japan. Furthermore, 2-methylimidazole with a purity of 97% and cobalt(II) nitrate hexahydrate ($Co(NO_3)_2 \cdot 6H_2O$) with a purity of 98% were purchased from Alfa Aesar. ZIF-67 nanoparticles were synthesized following the room-temperature synthesis method detailed in our previous study.[37] After this, the ZIF-67 nanoparticles were subjected to three rounds of washing via centrifugation and were finally dispersed in ethanol using a sonicator. This ethanolic suspension of nanoparticles was blended with a specific quantity of YSZ. Subsequently, the mixture was ball-milled (Retsch MM400) at 25 Hz for 30 min. The resulting homogeneous blend was dried via stirring and heating by using a magnetic stirrer. This process yielded powder mixtures denoted as YSZ/ZIF67-*x*, where *x* (1, 4, 7, and 10) represents the weight percentage of ZIF-67. The crystal structures of the starting materials are shown in Figure S1.

2.2. Sintering Process. Consolidation of the pure YSZ and hybrid powders (YSZ/ZIF67-*x*) was performed using SPS (FCT Systeme GmbH (Germany)). A uniaxial pressure of 50 MPa was applied, and the powders were heated to 1300 °C with a 5 min dwell time of the powders. To avoid any undesired reactions, graphite foils were carefully positioned between the powders and the inner wall of a 20 mm graphite die. The entire process was performed under vacuum ($<10^{-2}$ mbar) at a rapid heating rate of 100 °C/min. The temperature increment was meticulously regulated during sintering using a pulsed electrical current with 12 ms on and 2 ms off cycles. An optical pyrometer is used to monitor the temperature inside the graphite punch. After the sintering process was complete, the power was shut off and the furnace was allowed to cool naturally.

2.3. Structural Characterization. The bulk densities of the sintered specimens were determined by the Archimedes method using distilled water after removal of the graphite layers adhered to the surfaces of the specimens. The characterization of the phase analysis pertaining to the sintered samples was accomplished through the utilization of powder X-ray diffraction, covering the angular range spanning from 20 to 80° (2θ). This characterization involved specific instrumental settings, including 40 kV accelerating voltage, 15 mA current, 2° min^{-1} scanning speed, and a step size of 0.02. The microstructures of the sintered samples were examined by scanning electron microscopy from the fractured surfaces (SEM; Zeiss Ultra Plus). Further elemental analyses were carried out using energy-dispersive X-ray spectroscopy (EDS; Oxford Instruments, INCA ENERGY). Raman spectrum (WITec alpha300 RA-Oxford Instrument) of the sintered samples was performed on the fractured surfaces by utilizing a laser with a wavelength of 532 nm for excitation with a 100× objective lens.

2.4. Mechanical and Electrical Characterization. The Vickers hardness (HV10) of the sintered samples was measured using a Vickers hardness tester (EMCO Test, M1C, Germany) with a load of 10 kg by pressing a diamond indenter onto the surface of the samples for 3 s. The indentation size was then measured, and the Vickers hardness value was calculated using an empirical equation (see the Supporting Information (SI)). The KIC value was determined using the Evans and Charles method,[38] specifically by employing the indentation fracture (IF) technique from five indentation tests. This method involves measuring the lengths of the radial cracks that propagate from the corners of a Vickers indenter. These measured crack lengths were then used in an empirical equation based on the radial crack length produced by Vickers indentation.

The electrical resistivity of the samples was assessed by using two different approaches. The two-probe and four-probe van der Pauw methods were applied to the prepared samples. To prepare the samples, the external surfaces of sintered circular pieces measuring 20 mm in diameter and 3 mm in thickness were polished until they achieved a mirror-like finish. The samples were then subjected to a 60 nm thick gold deposition process to prevent ohmic loss. One side (lower) was completely coated, whereas four small contacts were placed at the corners of the other side (upper). In the two-probe method, the upper small contact and lower contact were used,

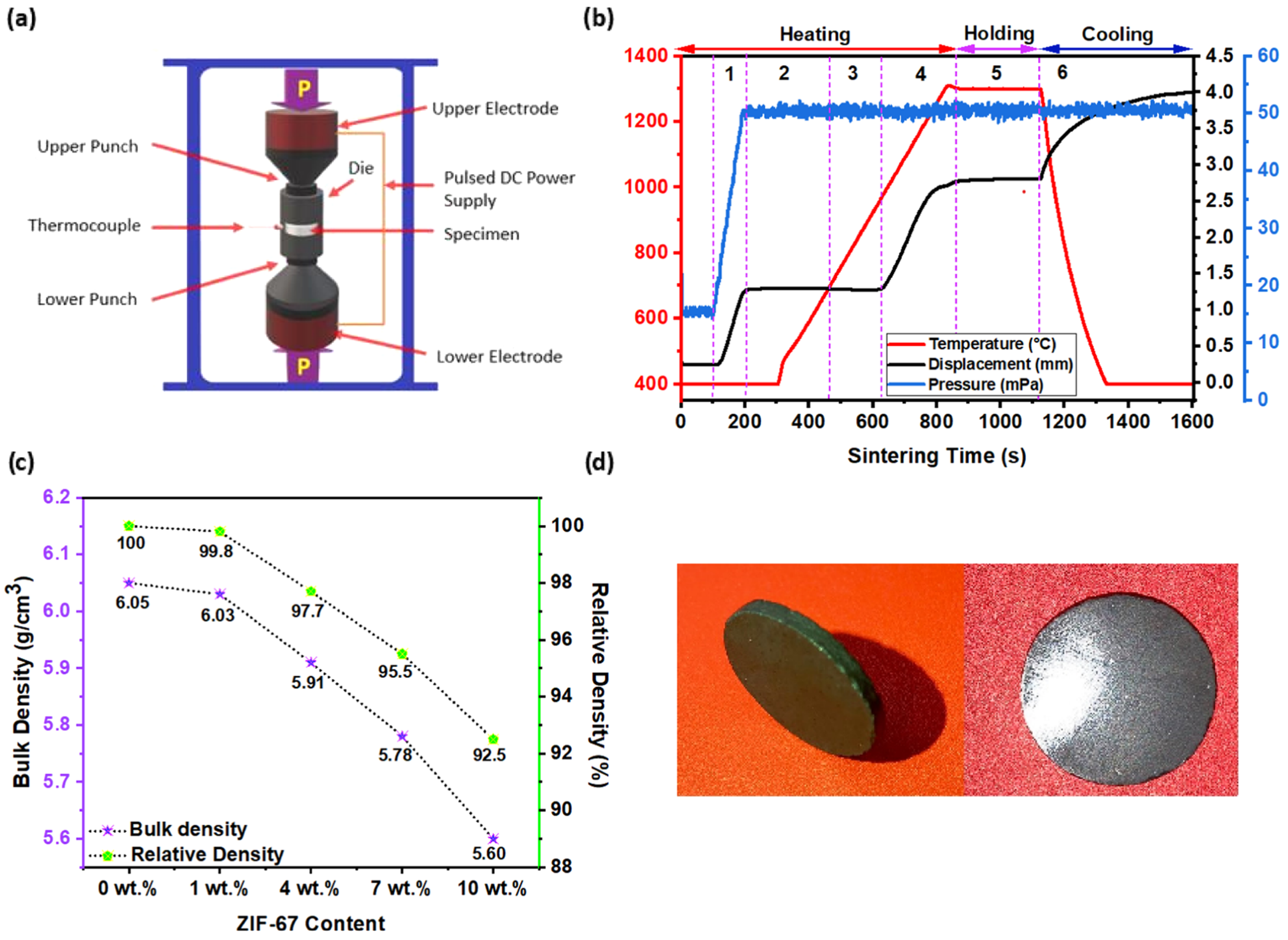

Figure 1. (a) Schematic of SPS setup. (b) SPS punch movement (displacement), sample temperature, and uniaxial pressure as a function of sintering time for YSZ/ZIF67−10. (c) Densities of the sintered samples. (d) Digital photographs of the sintered YSZ/ZIF67−10 composite.

whereas in the van der Pauw method, all four contacts on the upper surface were used.

3. RESULTS AND DISCUSSION

3.1. Structural Characterization. Figure 1a shows the main components of the SPS equipment. In the SPS process, the powders are subjected to a higher heating rate to quickly reach a high temperature. This accelerated sintering process facilitates powder densification. Rapid heating of the samples during SPS bypassed the low-temperature range where surface diffusion, a mechanism that does not promote densification, is active. Instead, it directly enters the elevated temperature range, where densification mechanisms such as the grain boundary and volume diffusion are predominant. Figure 1b shows the temperature and displacement compaction of the powders during consolidation in SPS. Thermal expansion was observed between the temperature ranges of 600 and 1300 °C. This behavior is mostly attributed to the decomposition of ZIF-67 (350−600 °C) and the formation of ZIF-67-derived nanocarbons and metallic Co.[39,40] Between 1000 and 1200 °C, a steady shrinkage displacement indicates ideal densification. The YSZ/ZIF67 powder compacted during the heating stage to a sintering temperature of 1300 °C, as is evident from the absence of further displacement increases during the holding period. The SPS process was concluded with a cooling stage.

The density of the sintered YSZ in this study is in good agreement with the reported density of pure zirconia of 6.05 g/cm^3.[41] The relative density of the YSZ/ZIF67 samples obtained by SPS at 1300 °C showed that as the ZIF-67 content increased, the relative density of the composites decreased (Figure 1c). This decrease could be attributed to the carbonization of ZIF-67 during sintering, which affects the packing efficiency of the composite material. When the amount of MOF-derived carbon in the ceramic matrix increases, achieving a uniform distribution of the carbon phase at the grain boundaries becomes challenging. This uneven distribution results in the local clustering of carbon particles known as agglomeration. Consequently, microdefects and permanent pores are formed, leading to a reduction in density.[42] The relative densities of the sintered composites were between 99.8 and 92.5%, implying that the compaction of the powders was good with low levels of porosity. Digital photographs of the highly shiny and monolithically produced samples confirm the carbonization of ZIF-67 (Figure 1d).

Prior to sintering, the as-received YSZ powder exhibits a combination of monoclinic and tetragonal phases, as indicated by the X-ray diffraction (XRD) peaks presented in Figure S2 and confirmed by formal analysis. The majority of XRD diffraction patterns align with the tetragonal phase (XRD PDF#82−1241), while diffraction peaks associated with the monoclinic phase are also observed, in accordance with the

https://doi.org/10.1021/acsami.3c15359
ACS Appl. Mater. Interfaces 2023, 15, 58931−58939

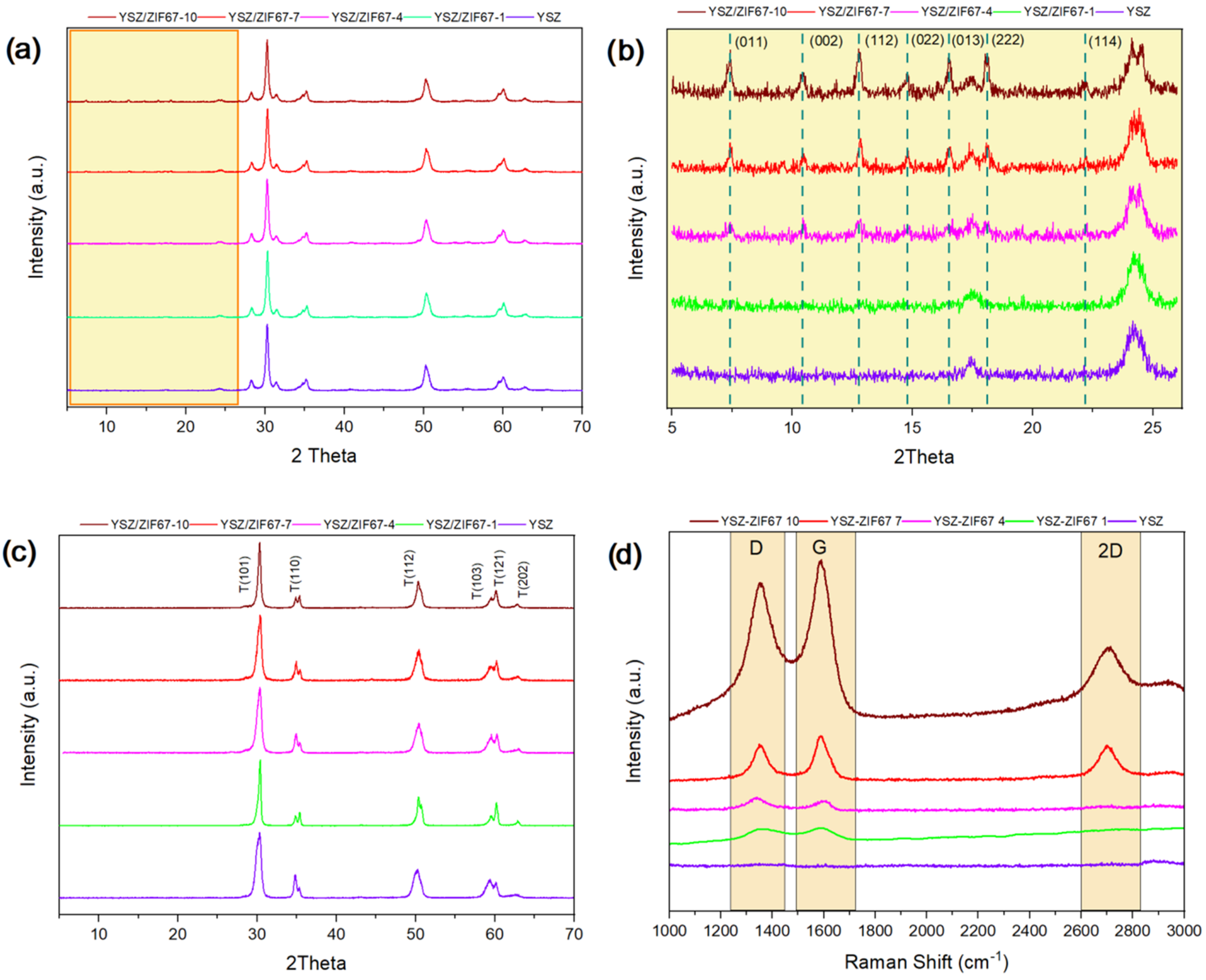

Figure 2. PXRD patterns of (a, b) YSZ/ZIF-67 powder mixtures before sintering and (c) sintered samples. (d) Raman spectra of the sintered samples.

XRD PDF card (XRD PDF#86−1449). The presence of this mixed phase in the initial powder may be attributed to the uneven distribution of Y within the YSZ nanopowders.[43] After sintering at 1300 °C, the diffraction peaks previously associated with the monoclinic phase no longer appear. This can be attributed to the uniform distribution achieved through high-temperature diffusion during the sintering process.[44] Regardless of the ZIF-67 content, all of the sintered ceramic composites are in the tetragonal phase. In the XRD patterns of YSZ/ZIF-67 powder mixtures, although the peak intensities are low due to the low amount of ZIF-67 in the precursors, characteristic peaks of ZIF-67 are observed (Figure 2a,b). This indicates that the ZIF-67 nanoparticles did not undergo amorphization and retained their crystallinity during the preparation of the samples, including the ball-milling process. Furthermore, nitrogen adsorption isotherms (Figure S3) and thermogravimetric analysis (Figure S4) of the powder mixtures were analyzed before sintering to confirm the stability of the added MOF. As anticipated, the surface area of the powder mixture increased directly with the amount of ZIF-67 present, reaching 142 m^2/g at the highest MOF content. However, the ZIF-67 peaks disappear in the XRD patterns after high-temperature sintering, as expected (Figure 2c). ZIF-67 undergoes thermolysis as a result of the high temperature during sintering and is transformed into carbon and cobalt nanoparticles. In particular, the peak at 28.2, which is clearly observed in the XRD pattern of the YSZ/ZIF67−10 sample with the highest ZIF-67 ratio, can be attributed to graphitic carbon (Figure S5).[45] Unlike the amorphous carbon derived from ZIFs at lower temperatures in the literature, this graphitic carbon formed by sintering is a result of the Co nanoparticles acting as a catalyst to graphitize the amorphous carbon and also the high sintering temperature (1300 °C) assisting the graphite formation process.[46] On the other hand, no characteristic peak directly attributable to Co nanoparticles could be observed in the XRD patterns owing to the lower Co content compared to the C content and also because the characteristic peaks of metallic Co overlap with those of YSZ. However, the formation of carbon allotropes and Co from the in situ thermolysis of ZIF-67 during the sintering process was evidenced by Raman spectroscopy and energy dispersive X-ray (EDX), as shown below.

The characteristic structure of the in situ ZIF-67-derived carbon in the YSZ composites was elucidated by Raman spectroscopy (Figure 2d). The Raman spectra of all YSZ/ZIF67 composites distinctly exhibit a G-band at 1587 cm^{-1}, which corresponds to the E_{2g} vibration mode of first-order scattering in sp^2-carbon materials.[47] A notable D-band at 1352 cm^{-1} (corresponding to the A_{1g} mode) was also observed, indicating the presence of disorder in the sp^2-carbon structure and highlighting the heightened level of defects within the graphitic carbon.[48] Additionally, the appearance of prominent two-dimensional (2D) bands at 2707 cm^{-1} provides evidence for the development of in situ graphitic structures in sintered composites. The relationship between the intensities of the well-separated G and D bands (I_D/I_G) in the Raman spectra also plays a crucial role in gauging the extent of graphitic carbon crystallization. In our samples, the relative intensity ratios of the G to D bands (I_G/I_D) became 1.15 as the amount of in situ ZIF-67-derived carbon increases, implying that a large number of defects were generated during the sintering (SPS) process.[49] Simultaneously, the intensity of the 2D band increases, which further confirms that the graphite structures are well developed. As a result, the existence of graphitic carbon in the composites, owing to the very high sintering temperature and the catalytic effect of the resulting Co particles, was revealed by Raman spectroscopy.

3.2. Microstructure and Mechanical Properties. SEM images of the fracture surfaces of YSZ and YSZ/ZIF-67 composites are shown in Figure 3. While the grain size of pure YSZ is approximately 300 nm, the grain size decreases significantly with an increase in the amount of ZIF-67-derived nanocarbon in the composites. For example, the grain size of YSZ/ZIF-67−4 is 150 nm, while it is smaller than 100 nm for YSZ/ZIF67−10. These observations are likely attributed to the widely employed technique of fine-grain strengthening, which is a common method used to enhance the strength and resilience of ceramic composites by incorporating nanocarbon. In this method, nanocarbons tend to aggregate along grain boundaries, yielding a stabilizing influence that not only facilitates the dispersion of nanocarbons within the composite but also hinders the growth of grains.[50] SEM micrographs corroborate this argument by demonstrating the presence of ZIF-67-derived nanocarbons situated at grain boundaries (Figure 3b,e). Notably, it has been reported that the shape of nanocarbons within the ceramic matrix composite exerts a pronounced influence on grain growth and, consequently, mechanical properties. In addition to the pinning effect, the presence of nanocarbons with high aspect ratios, such as graphene, entwined at grain boundaries, can effectively impede grain growth.[51] Therefore, the decrease in the grain size can also be attributed to the layered graphitic nature of the ZIF-67-derived nanocarbon formed during sintering. As depicted in Figure 3, the morphology of the grains within the composite underwent alterations in addition to changes in grain size with increasing ZIF-67-derived nanocarbon content. Notably, pure sintered YSZ exhibits grains with sharp faceted edges, which are common characteristics of sintered ceramics. However, as the nanocarbon concentration in the composites increases, particularly in YSZ/ZIF67−10, which has the highest carbon content, these sharp faceted edges often transform into blunter profiles. Typically, this grain morphology is observed during the initial stages of sintering. This phenomenon can be attributed to the anisotropic surface energy of the ceramic, where grains evolve to attain equilibrium, resulting in zero boundary curvature for alumina.[52] In fact, it is unusual for ceramics to densify without boundary regions reaching dynamic equilibrium. This observation suggests that the grain edges enveloped by nanoporous carbon remained rounded, inhibiting zirconia grain growth from filling the triple point. Energy-dispersive X-ray spectroscopy (EDS) analysis, as depicted in Figure S6, confirms the presence of Co in the composite. Considering the higher evaporation temperature of Co compared to the sintering temperature employed, it is expected to remain within the matrix. The existing literature supports the rationale behind Co retention in the composite.[53]

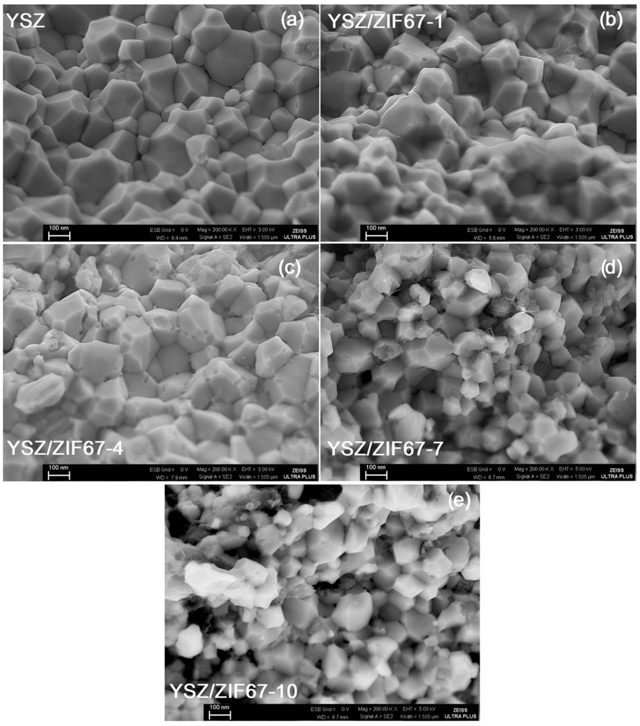

Figure 3. SEM images of the fractured surfaces of the sintered samples. (a) Pure YSZ, (b) YSZ/ZIF67−1, (c) YSZ/ZIF67−4, (d) YSZ/ZIF67−7, and (e) YSZ/ZIF67−10.

Table 1. Hardness, Toughness, and Electrical Conductivity of the Sintered Samples

sample	hardness (GPa)	toughness (MPa·$m^{1/2}$)	conductivity (S/m) two-probe	conductivity (S/m) van der Pauw
YSZ	13.06	5.10	2.4×10^{-8}	
YSZ/ZIF67−1	12.78	5.14	5.2×10^{-8}	
YSZ/ZIF67−4	10.99	5.19	0.02	3.09×10^{-3}
YSZ/ZIF67−7	10.40	5.73	1.61	3.01×10^{-1}
YSZ/ZIF67−10	8.53	5.77	27	6.82×10^{-1}

The room-temperature mechanical characteristics of the sintered specimens were assessed by measuring their hardness and fracture toughness (Table 1 and Figure 4a). The reported values in Table 1 are the averages of the data from five indentation tests for the hardness measurement. The Vickers hardness (HV) value measured for sintered pure YSZ (13.06 GPa) is in very good agreement with the literature.[54] The results show that HV decreased with increasing ZIF-67 content, and the mechanical hardness of YSZ/ZIF67−10 decreased by 35% compared to that of pure YSZ. This is

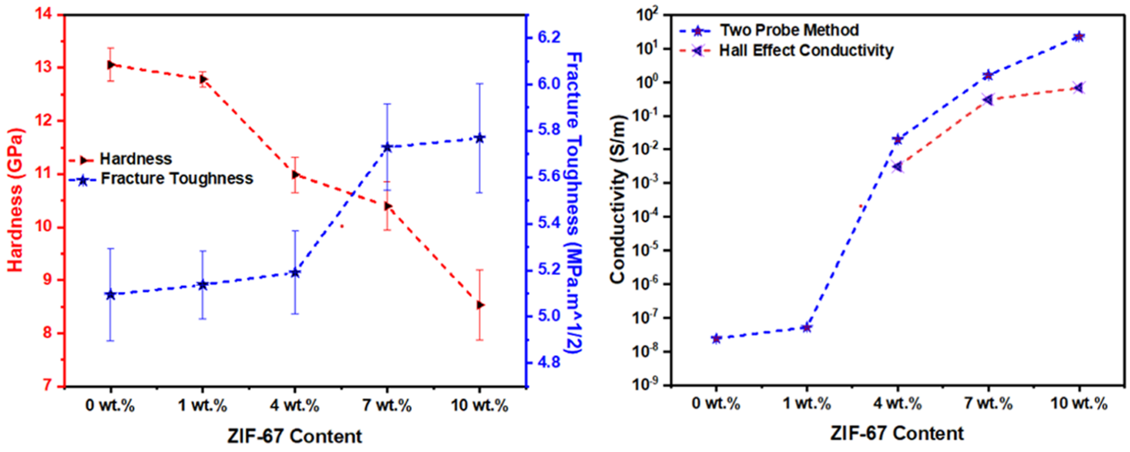

Figure 4. (a) Mechanical and (b) electrical properties of the sintered samples as a function of ZIF-67 content.

reasonable because the Vickers hardness is affected by the relative density. The impact of pores on the hardness of a ceramic is the most detrimental; therefore, much of the decrease in HV is attributable to an increase in porosity. However, the greater decrease in HV compared to the density can be attributed to the presence of soft nanocarbon phases at the grain boundaries and the self-lubricating properties of the sheet-like carbons.[50]

The results clearly demonstrate a substantial enhancement in the fracture toughness of the composite samples, notably reaching an improvement of up to 13.2% for YSZ/ZIF67−10 compared to pure YSZ. This gradual improvement in the fracture toughness is exhibited up to a certain ZIF-67 ratio. Beyond this point, a sharp increase is observed with higher ZIF-67 ratios, followed by a more gradual rate of increase as the reinforcement phase volume increases. This observation is consistent with previous reports of numerous CMCs. It has been documented that an increased proportion of nanocarbon reinforcement can lead to deterioration in toughness. This phenomenon is primarily attributed to higher nanocarbon reinforcement within an elevated ceramic matrix, which results in agglomeration and the formation of pores in the ceramic structure.[50] Moreover, greater reinforcement material can intensify the contact between graphitic carbon plates, creating pathways between weakly bonded planes and consequently contributing to the rapid propagation of cracks.[55] The significant enhancement in fracture toughness can be attributed to the presence of ZIF-67-derived graphitic carbon within the composites, which serves as a pivotal agent for both crack deflection and crack bridging. Crack deflection describes the process by which a propagating crack tilts and twists, deviating from its original path as it encounters the reinforcing nanocarbon situated at the fragile interface formed with the matrix. The crack-bridging mechanism functions by generating closure forces as a result of the resistance encountered by partially detached nanocarbon fillers, coupled with their mechanical interlocking with the matrix.[55] Indeed, SEM images depicting radial cracks growing at the corners of the Vickers indentation corroborate that the enhancement in fracture toughness in YSZ/ZIF-67 composites can be attributed to these dual mechanisms (Figure S7).

3.3. Electrical Properties. Various studies have investigated the electrical conductivity of sintered composite materials based on zirconia, both partially and fully stabilized, doped with different carbon additives.[56] These composites demonstrated a consistent level of electronic conductivity over time, even under challenging conditions involving high temperatures and oxygen exposure.[57] Despite this, the impact of incorporating various types of carbon materials on the electrical conductivity and the point at which percolation becomes significant have not been clearly delineated. The reported values differ notably from one study to another. One apparent factor contributing to this variability is the distinct concentration of Y_2O_3 dopant present within the zirconia matrix.[58] It is worth noting that the zirconia matrix displays varying capabilities for hole doping, in the order of 3YTZP (partially stabilized with 3 mol % Y_2O_3) followed by 8YSZ (fully stabilized with 8 mol % Y_2O_3). This discrepancy arises from the different levels of anion vacancies in these materials. Numerous other considerations further shape the electrical behavior of these composites. These include the type of carbon derivative employed, characteristics of the zirconia precursor (particle size distribution, specific surface area, etc.), and techniques employed during the processing phase. In this study, the electrical conductivities of the sintered composites were examined by using two distinct methods.

The electrical conductivity results obtained at room temperature are depicted in Figure 4b in relation to the ZIF-67 content. The conductivities of pure YSZ and the composites were scrutinized using the two-probe technique by increasing the percentage of the second phase in the matrix. The conductivity of the composites increases rather slowly with the addition of 1 wt % ZIF-67, reaching a value of 5×10^{-8} Sm^{1-}. A gradual increase in the amount of MOF-derived carbon drastically enhances the electrical conductivities of the composite samples. The YSZ/ZIF67−10 composite exhibits a conductivity of 27 Sm^{1-}, which is one of the highest comparable values reported in the literature for zirconia matrix composites at room temperature, confirming that the MOF-derived carbons created an interconnected conductive network, resulting in an electron pathway throughout the bulk material. Consequently, the multitude of mobile charge carriers that permeate the interconnected system leads to an increased conductivity. Pure YSZ, which has an extremely low electrical conductivity in the range of 10^{-8} Sm^{1-}, experiences an insulator-to-conductor transition with a maximum conductivity of 9 orders of magnitude. The high electrical conductivity acquired by the low carbon ratio is attributed to the rich nitrogen content of ZIF-67. In the Hall effect conductivity measurement of the pure ceramic up to YSZ/ZIF67−1 composites, no results could be achieved because the conductivity was beyond certain limits of the instrument. Although the conductivity values were not particularly elevated, it was observed that as the content of MOF-derived carbon in the matrix increased, correspondingly elevated conductivity values were recorded. The variations in the conductivity measurements are due to the anisotropic nature of the samples, which is highly dependent on the measurement technique performed. When the two-probe method is utilized, voltage is applied perpendicular to the surface of the sample, whereas in the measurement of the Hall effect conductivity, it is applied parallel to the surface.

4. CONCLUSIONS

In conclusion, our study represents a pioneering step in exploring MOF-derived nanocarbons as reinforcement phases in CMCs. Our findings demonstrate that the integration of zeolitic imidazolate framework (ZIF-67)-derived nanocarbons into yttria-stabilized zirconia (YSZ) matrices leads to substantial improvements in fracture toughness and electrical conductivity. The formation of ZIF-derived nanocarbon interlayers plays a critical role in enhancing fracture toughness by facilitating energy dissipation during crack propagation and restraining grain growth. Furthermore, the noteworthy room-temperature electrical conductivity achieved in these composites not only allows for various applications but also emphasizes the potential identified in this study. In particular, in the field of solid-state electrochemical applications, such as fuel cell electrode processes and oxygen sensors, the electrical conductivity obtained in this study is promising. Future investigations may concentrate on optimizing the sintering parameters and composition of nanocarbon-reinforced CMCs to enhance their overall performance. In addition, investigating the scalability and industrial viability of this approach is crucial for its successful integration into practical applications across various industries. Overall, the incorporation of MOF-derived nanocarbons holds tremendous promise in revolutionizing the landscape of advanced materials with enhanced mechanical, electrical, and thermal properties.

■ ASSOCIATED CONTENT

Supporting Information

The Supporting Information is available free of charge at https://pubs.acs.org/doi/10.1021/acsami.3c15359.

> Additional XRD patterns; EDX spectra of sintered samples; crack propagation profiles; hardness, and fracture toughness calculation equations (PDF)

■ AUTHOR INFORMATION

Corresponding Authors

Mustafa Erkartal − *Department of Engineering Science, Faculty of Engineering, Abdullah Gul University, Kayseri 38080, Turkey;* orcid.org/0000-0002-9772-128X; Email: mustafa.erkartal@agu.edu.tr

Unal Sen − *Department of Materials Science and Engineering, Faculty of Engineering, Eskisehir Technical University, Eskisehir 26555, Turkey; Advanced Technologies Application and Research Center, Eskisehir Technical University, Eskisehir 26555, Turkey;* orcid.org/0000-0003-3736-5049; Email: unalsen@eskisehir.edu.tr

Authors

Niyaz Cakan − *Department of Materials Science and Engineering, Faculty of Engineering, Eskisehir Technical University, Eskisehir 26555, Turkey*

Abduselam Abubeker Issa − *Department of Materials Science and Engineering, Faculty of Engineering, Eskisehir Technical University, Eskisehir 26555, Turkey*

Hamza Alsalman − *Department of Mechanical Engineering, Faculty of Engineering, Abdullah Gul University, Kayseri 38080, Turkey*

Emin Aliyev − *Department of Mechanical Engineering, Faculty of Engineering, Abdullah Gul University, Kayseri 38080, Turkey; UNAM−Institute of Materials Science and Nanotechnology, Bilkent University, Ankara 06800, Turkey*

Enes Ibrahim Duden − *Department of Materials Science and Engineering, Faculty of Engineering, Eskisehir Technical University, Eskisehir 26555, Turkey;* orcid.org/0000-0003-4025-3101

Kubra Gurcan Bayrak − *Department of Materials Science and Engineering, Faculty of Engineering, Eskisehir Technical University, Eskisehir 26555, Turkey*

Mujdat Caglar − *Department of Physics, Faculty of Science, Eskisehir Technical University, Eskisehir 26470, Turkey;* orcid.org/0000-0001-9724-7664

Servet Turan − *Department of Materials Science and Engineering, Faculty of Engineering, Eskisehir Technical University, Eskisehir 26555, Turkey;* orcid.org/0000-0002-7322-3091

Complete contact information is available at: https://pubs.acs.org/10.1021/acsami.3c15359

Author Contributions

$^{\nabla}$N.C., A.A.I., H.A., and E.A. contributed equally to this work.

Notes

The authors declare no competing financial interest.

■ ACKNOWLEDGMENTS

The Scientific and Technological Research Council of Turkey (TUBITAK) provided funding for this project (grant number: 222M085).

■ REFERENCES

(1) Ashby, M. F.; Cebon, D. Materials selection in mechanical design. *J. Phys. IV* **1993**, *03* (C7), C7-1−C7-9.

(2) Bouville, F.; Maire, E.; Meille, S.; Van de Moortele, B.; Stevenson, A. J.; Deville, S. Strong, tough and stiff bioinspired ceramics from brittle constituents. *Nat. Mater.* **2014**, *13* (5), 508−514.

(3) Zhang, X.; Zhao, N. Q.; He, C. N. The superior mechanical and physical properties of nanocarbon reinforced bulk composites achieved by architecture design - A review. *Prog. Mater. Sci.* **2020**, *113*, No. 100672, DOI: 10.1016/j.pmatsci.2020.100672.

(4) Wang, J.; Deng, X.; Du, S.; Cheng, F.; Li, F.; Lu, L.; Zhang, H. Carbon Nanotube Reinforced Ceramic Composites: A Review. *Interceram - Int. Ceram. Rev.* **2014**, *63* (6), 286−289.

(5) Sun, J. X.; Ye, D. R.; Zou, J.; Chen, X. T.; Wang, Y.; Yuan, J. S.; Liang, H. W.; Qu, H. Q.; Binner, J.; Bai, J. M. A review on additive manufacturing of ceramic matrix composites. *J. Mater. Sci. Technol.* **2023**, *138*, 1−16.

(6) Walker, L. S.; Marotto, V. R.; Rafiee, M. A.; Koratkar, N.; Corral, E. L. Toughening in Graphene Ceramic Composites. *ACS Nano* **2011**, *5* (4), 3182−3190.

(7) Luo, B. C.; Wang, X. H.; Tian, E. K.; Gong, H. L.; Zhao, Q. C.; Shen, Z. B.; Xu, Y.; Xiao, X. Y.; Li, L. Dielectric Enhancement in

Graphene/Barium Titanate Nanocomposites. *ACS Appl. Mater. Interfaces* **2016**, *8* (5), 3340−3348.

(8) Liu, J.; Yang, Y.; Hassanin, H.; Jumbu, N.; Deng, S. A.; Zuo, Q.; Jiang, K. L. Graphene-Alumina Nanocomposites with Improved Mechanical Properties for Biomedical Applications. *ACS Appl. Mater. Interfaces* **2016**, *8* (4), 2607−2616.

(9) Zhan, G. D.; Kuntz, J. D.; Wan, J. L.; Mukherjee, A. K. Single-wall carbon nanotubes as attractive toughening agents in alumina-based nanocomposites. *Nat. Mater.* **2003**, *2* (1), 38−42.

(10) Sang, G. L.; Wang, C.; Zhao, Y.; He, G.; Zhang, Q. F.; Yang, M. H.; Zhao, S. H.; Xu, P.; Xi, X. Q.; Yang, J. L. Ni@CNTs/Al2O3 Ceramic Composites with Interfacial Solder Strengthen the Segregated Network for High Toughness and Excellent Electromagnetic Interference Shielding. *ACS Appl. Mater. Interfaces* **2022**, *14* (3), 4443−4455.

(11) Shi, Z. Q.; Chen, S. G.; Wang, J. P.; Qiao, G. J.; Jin, Z. H. Mechanical and electrical properties of carbon nanofibers reinforced aluminum nitride composites prepared by plasma activated sintering. *J. Eur. Ceram. Soc.* **2011**, *31* (12), 2137−2143.

(12) Cano-Crespo, R.; Moshtaghioun, B. M.; Gomez-Garcia, D.; Dominguez-Rodriguez, A.; Moreno, R. High-temperature creep of carbon nanofiber-reinforced and graphene oxide-reinforced alumina composites sintered by spark plasma sintering. *Ceram. Int.* **2017**, *43* (9), 7136−7141.

(13) Morales-Flórez, V.; Domínguez-Rodríguez, A. Mechanical properties of ceramics reinforced with allotropic forms of carbon. *Prog. Mater. Sci.* **2022**, *128*, No. 100966, DOI: 10.1016/j.pmatsci.2022.100966.

(14) Xia, H. Y.; Zhang, X.; Shi, Z. Q.; Zhao, C. J.; Li, Y. F.; Wang, J. P.; Qiao, G. J. Mechanical and thermal properties of reduced graphene oxide reinforced aluminum nitride ceramic composites. *Mater. Sci. Eng.: A* **2015**, *639*, 29−36.

(15) Zhang, S. C.; Fahrenholtz, W. G.; Hilmas, G. E.; Yadlowsky, E. J. Pressureless sintering of carbon nanotube-Al2O3 composites. *J. Eur. Ceram. Soc.* **2010**, *30* (6), 1373−1380.

(16) Furukawa, H.; Cordova, K. E.; O'Keeffe, M.; Yaghi, O. M. The Chemistry and Applications of Metal-Organic Frameworks. *Science* **2013**, *341* (6149), No. 1230444.

(17) Chen, Z. J.; Kirlikovali, K. O.; Li, P.; Farha, O. K. Reticular Chemistry for Highly Porous Metal-Organic Frameworks: The Chemistry and Applications. *Acc. Chem. Res.* **2022**, *55* (4), 579−591.

(18) Bennett, T. D.; Horike, S. Liquid, glass and amorphous solid states of coordination polymers and metal-organic frameworks. *Nat. Rev. Mater.* **2018**, *3* (11), 431−440.

(19) Erkartal, M.; Sen, U. Boronic Acid Moiety as Functional Defect in UiO-66 and Its Effect on Hydrogen Uptake Capacity and Selective CO2 Adsorption: A Comparative Study. *ACS Appl. Mater. Interfaces* **2018**, *10* (1), 787−795.

(20) Chen, Z. J.; Mian, M. R.; Lee, S. J.; Chen, H. Y.; Zhang, X.; Kirlikovali, K. O.; Shulda, S.; Melix, P.; Rosen, A. S.; Parilla, P. A.; Gennett, T.; Snurr, R. Q.; Islamoglu, T.; Yildirim, T.; Farha, O. K. Fine-Tuning a Robust Metal-Organic Framework toward Enhanced Clean Energy Gas Storage. *J. Am. Chem. Soc.* **2021**, *143* (45), 18838−18843.

(21) Qazvini, O. T.; Scott, V. J.; Bondorf, L.; Ducamp, M.; Hirscher, M.; Coudert, F. X.; Telfer, S. G. Flexibility of a Metal-Organic Framework Enhances Gas Separation and Enables Quantum Sieving. *Chem. Mater.* **2021**, *33* (22), 8886−8894.

(22) Fan, W. D.; Ying, Y. P.; Peh, S. B.; Yuan, H. Y.; Yang, Z. Q.; Yuan, Y. D.; Shi, D. C.; Yu, X.; Kang, C. J.; Zhao, D. Multivariate Polycrystalline Metal-Organic Framework Membranes for CO2/CH4 Separation. *J. Am. Chem. Soc.* **2021**, *143* (42), 17716−17723.

(23) Wang, S. J.; Ly, H. G. T.; Wahiduzzaman, M.; Simms, C.; Dovgaliuk, I.; Tissot, A.; Maurin, G.; Parac-Vogt, T. N.; Serre, C. A zirconium metal-organic framework with SOC topological net for catalytic peptide bond hydrolysis. *Nat. Commun.* **2022**, *13* (1), No. 1284, DOI: 10.1038/s41467-022-28886-5.

(24) Lázaro, I. A.; Forgan, R. S.; Cirujano, F. G. MOF nanoparticles as heterogeneous catalysts for direct amide bond formations. *Dalton Trans.* **2022**, *51* (21), 8368−8376.

(25) Safa, S.; Khajeh, M.; Oveisi, A. R.; Azimirad, R. Graphene quantum dots incorporated UiO-66-NH as a promising photocatalyst for degradation of long-chain oleic acid. *Chem. Phys. Lett.* **2021**, *762*, No. 138129, DOI: 10.1016/j.cplett.2020.138129.

(26) Daliran, S.; Oveisi, A. R.; Peng, Y.; López-Magano, A.; Khajeh, M.; Mas-Ballesté, R.; Alemán, J.; Luque, R.; Garcia, H. Metal−organic framework (MOF)-, covalent-organic framework (COF)-, and porous-organic polymers (POP)-catalyzed selective C−H bond activation and functionalization reactions. *Chem. Soc. Rev.* **2022**, *51* (18), 7810−7882.

(27) Sen, U.; Erkartal, M.; Kung, C. W.; Ramani, V.; Hupp, J. T.; Farha, O. K. Proton Conducting Self-Assembled Metal-Organic Framework/Polyelectrolyte Hollow Hybrid Nanostructures. *ACS Appl. Mater. Interfaces* **2016**, *8* (35), 23015−23021.

(28) Sheberla, D.; Bachman, J. C.; Elias, J. S.; Sun, C. J.; Shao-Horn, Y.; Dinca, M. Conductive MOF electrodes for stable supercapacitors with high areal capacitance. *Nat. Mater.* **2017**, *16* (2), 220−224.

(29) Wang, H. F.; Chen, L. Y.; Pang, H.; Kaskel, S.; Xu, Q. MOF-derived electrocatalysts for oxygen reduction, oxygen evolution and hydrogen evolution reactions. *Chem. Soc. Rev.* **2020**, *49* (5), 1414−1448.

(30) Zhang, H.; Liu, X. M.; Wu, Y.; Guan, C.; Cheetham, A. K.; Wang, J. MOF-derived nanohybrids for electrocatalysis and energy storage: current status and perspectives. *Chem. Commun.* **2018**, *54* (42), 5268−5288.

(31) Duden, E. I.; Bayrak, K. G.; Balkan, M.; Cakan, N.; Demiroglu, A.; Ayas, E.; Caglar, M.; Turan, S.; Islamoglu, T.; Farha, O. K.; Erkartal, M.; Sen, U. Boosting the Ceramics with In Situ MOF-Derived Nanocarbons. *ACS Mater. Lett.* **2023**, *5* (6), 1537−1545.

(32) Grech, J.; Antunes, E. Zirconia in dental prosthetics: a literature review. *J. Mater. Res. Technol.* **2019**, *8* (5), 4956−4964.

(33) Zakaria, Z.; Hassan, S. H. A.; Shaari, N.; Yahaya, A. Z.; Kar, Y. B. A review on recent status and challenges of yttria stabilized zirconia modification to lowering the temperature of solid oxide fuel cells operation. *Int. J. Energy Res.* **2020**, *44* (2), 631−650.

(34) Dvilis, E. S.; Paigin, V. D.; Stepanov, S. A.; Khasanov, O. L.; Valiev, D. T.; Polisadova, E. F.; Vaganov, V.; Alishin, T. R.; Dudina, D. V. Effect of Spark Plasma Sintering Temperature on the Properties of Transparent YSZ Ceramics. *Refract. Ind. Ceram.* **2019**, *60* (2), 154−159.

(35) Jang, B. K.; Lee, J. H.; Fisher, C. A. J. Mechanical properties and phase-transformation behavior of carbon nanotube-reinforced yttria-stabilized zirconia composites. *Ceram. Int.* **2021**, *47* (24), 35287−35293.

(36) Duan, C. X.; Yu, Y.; Hu, H. Recent progress on synthesis of ZIF-67-based materials and their application to heterogeneous catalysis. *Green Energy Environ.* **2022**, *7* (1), 3−15.

(37) Erkartal, M.; Erkilic, U.; Tam, B.; Usta, H.; Yazaydin, O.; Hupp, J. T.; Farha, O. K.; Sen, U. From 2-methylimidazole to 1,2,3-triazole: a topological transformation of ZIF-8 and ZIF-67 by post-synthetic modification. *Chem. Commun.* **2017**, *53* (12), 2028−2031.

(38) Evans, A. G.; Charles, E. A. Fracture Toughness Determinations by Indentation. *J. Am. Ceram. Soc.* **1976**, *59* (7−8), 371−372.

(39) Tang, J.; Salunkhe, R. R.; Liu, J.; Torad, N. L.; Imura, M.; Furukawa, S.; Yamauchi, Y. Thermal Conversion of Core-Shell Metal-Organic Frameworks: A New Method for Selectively Functionalized Nanoporous Hybrid Carbon. *J. Am. Chem. Soc.* **2015**, *137* (4), 1572−1580.

(40) Wang, S. Y.; Ke, X.; Zhong, S. T.; Lai, Y. R.; Qian, D. T.; Wang, Y. P.; Wang, Q. H.; Jiang, W. Bimetallic zeolitic imidazolate frameworks-derived porous carbon-based materials with efficient synergistic microwave absorption properties: the role of calcining temperature. *Rsc Adv.* **2017**, *7* (73), 46436−46444.

(41) Zeng, Z. Y. B.; Liu, Y. Z.; Chen, W. P.; Li, X. Q.; Zheng, Q. F.; Li, K. L.; Guo, R. R. Fabrication and properties of in situ reduced

graphene oxide-toughened zirconia composite ceramics. *J. Am. Ceram. Soc.* **2018**, *101* (8), 3498−3507.

(42) Harmer, M. A.; Brook, R. J. Fast firing-microstructural benefits. *Trans. J. Br. Ceram. Soc.* **1981**, *80*, No. 147.

(43) Ahmed, S.; Li, B.; Zou, L. F. Sintering of free-standing zirconia granules with different Y2O3 concentration. *Adv. Appl. Ceram.* **2020**, *119* (7), 407−413.

(44) Matsui, K.; Yoshida, H.; Ikuhara, Y. Review: microstructure-development mechanism during sintering in polycrystalline zirconia. *Int. Mater. Rev.* **2018**, *63* (6), 375−406.

(45) Shcherban, N. D.; Mäki-Arvela, P.; Aho, A.; Sergiienko, S. A.; Yaremov, P. S.; Eränen, K.; Murzin, D. Y. Melamine-derived graphitic carbon nitride as a new effective metal-free catalyst for Knoevenagel condensation of benzaldehyde with ethylcyanoacetate. *Catal. Sci. Technol.* **2018**, *8* (11), 2928−2937.

(46) You, B.; Jiang, N.; Sheng, M.; Drisdell, W. S.; Yano, J.; Sun, Y. Bimetal−Organic Framework Self-Adjusted Synthesis of Support-Free Nonprecious Electrocatalysts for Efficient Oxygen Reduction. *ACS Catal.* **2015**, *5* (12), 7068−7076.

(47) Sfyris, D.; Sfyris, G.; Galiotis, C. Stress intrepretation of graphene E-2g and A-1g vibrational modes: theoretical analysis, arXiv:1706.04465. arXiv.org e-Print archive, 2017. https://doi.org/10.48550/arXiv.1706.04465.

(48) Ru, J.; Fan, Y.; Zhou, W.; Zhou, Z.; Wang, T.; Liu, R.; Yang, J.; Lu, X.; Wang, J.; Ji, C.; et al. Electrically conductive and mechanically strong graphene/mullite ceramic composites for high-performance electromagnetic interference shielding. *Acs Appl. Mater. Interfaces* **2018**, *10* (45), 39245−39256.

(49) Liu, Y.; Xu, X.; Wang, M.; Lu, T.; Sun, Z.; Pan, L. Metal−organic framework-derived porous carbon polyhedra for highly efficient capacitive deionization. *Chem. Commun.* **2015**, *51* (60), 12020−12023.

(50) Liu, Y.; Jiang, X.; Shi, J.; Luo, Y.; Tang, Y.; Wu, Q.; Luo, Z. Research on the interface properties and strengthening−toughening mechanism of nanocarbon-toughened ceramic matrix composites. *Nanotechnol. Rev.* **2020**, *9* (1), 190−208.

(51) Shin, J.-H.; Choi, J.; Kim, M.; Hong, S.-H. Comparative study on carbon nanotube- and reduced graphene oxide-reinforced alumina ceramic composites. *Ceram. Int.* **2018**, *44* (7), 8350−8357.

(52) Fan, Y.; Estili, M.; Igarashi, G.; Jiang, W.; Kawasaki, A. The effect of homogeneously dispersed few-layer graphene on microstructure and mechanical properties of Al2O3 nanocomposites. *J. Eur. Ceram. Soc.* **2014**, *34* (2), 443−451.

(53) Tang, J.; Salunkhe, R. R.; Liu, J.; Torad, N. L.; Imura, M.; Furukawa, S.; Yamauchi, Y. Thermal Conversion of Core−Shell Metal−Organic Frameworks: A New Method for Selectively Functionalized Nanoporous Hybrid Carbon. *J. Am. Chem. Soc.* **2015**, *137* (4), 1572−1580.

(54) Arunkumar, T.; Anand, G.; Subbiah, R.; Karthikeyan, R.; Jeevahan, J. Effect of Multiwalled Carbon Nanotubes on Improvement of Fracture Toughness of Spark-Plasma-Sintered Yttria-Stabilized Zirconia Nanocomposites. *J. Mater. Eng. Perform.* **2021**, *30* (6), 3925−3933.

(55) Ramirez, C. 10 years of research on toughness enhancement of structural ceramics by graphene (vol 380, 20220006, 2022). *Philos. Trans. R. Soc., A* **2022**, *380* (2236), No. 20220006, DOI: 10.1098/rsta.2022.0006.

(56) Kurapova, O. Y.; Glukharev, A. G.; Glumov, O. V.; Kurapov, M. Y.; Boltynjuk, E. V.; Konakov, V. G. Structure and electrical properties of YSZ-rGO composites and YSZ ceramics, obtained from composite powder. *Electrochim. Acta* **2019**, *320*, No. 134573.

(57) Marinha, D.; Belmonte, M. Mixed-ionic and electronic conduction and stability of YSZ-graphene composites. *J. Eur. Ceram. Soc.* **2019**, *39* (2−3), 389−395.

(58) Fan, Y.; Kang, L.; Zhou, W.; Jiang, W.; Wang, L.; Kawasaki, A. Control of doping by matrix in few-layer graphene/metal oxide composites with highly enhanced electrical conductivity. *Carbon* **2015**, *81*, 83−90.